Optimal swimming with body compliance in an overdamped medium

Jianfeng Lin,[1,2,*] Tianyu Wang,[1,3,4,*] Baxi Chong,[5] Matthew Fernandez,[3] Zhaochen Xu,[1,2] and Daniel I. Goldman[1,†]

[1] *School of Physics, Georgia Institute of Technology, Atlanta, Georgia, USA*
[2] *Interdisciplinary Graduate Program in Quantitative Biosciences, Georgia Institute of Technology, Atlanta, Georgia, USA*
[3] *George W. Woodruff School of Mechanical Engineering, Georgia Institute of Technology, Atlanta, Georgia, USA*
[4] *Institute for Robotics and Intelligent Machines, Georgia Institute of Technology, Atlanta, Georgia, USA*
[5] *Department of Mechanical Engineering, The Pennsylvania State University, University Park, Pennsylvania, USA*

(Received 3 October 2025; revised 13 February 2026; accepted 3 April 2026; published 27 May 2026)

Elongate animals and robots use undulatory body waves to locomote through diverse environments. Geometric mechanics provides a framework to model and optimize such systems in highly damped environments, connecting a prescribed shape change pattern (gait) with locomotion displacement. However, the practical applicability of controlling compliant physical robots remains to be demonstrated. In this work, we develop a framework based on geometric mechanics to predict locomotor performance and search for optimal swimming strategies of compliant swimmers. We introduce a compliant extension of Purcell's three-link swimmer by incorporating series-connected springs at the joints. Body dynamics are derived with the use of resistive force theory. Geometric mechanics is incorporated into movement prediction and into an optimization framework that identifies strategies for controlling compliant swimmers to achieve maximal displacement. We validate our framework on a physical cable-driven, three-link limbless robot and demonstrate accurate prediction and optimization of locomotor performance under varied programmed, state-dependent compliance in a granular medium. Our results establish a systematic, physics-based approach for modeling and controlling compliant swimming locomotion, highlighting compliance as a design feature that can be exploited for robust movement in both homogeneous and heterogeneous environments.

DOI: 10.1103/pbkh-py5h

I. INTRODUCTION

Undulatory locomotion, in which traveling body waves generate self-propulsion, is a fundamental strategy used by elongate animals (e.g., snakes [1–5], eels [6,7], and skinks [8,9]) and robots [10–16] to traverse both fluid and terrestrial environments. These locomotive capabilities emerge from the interplay between body dynamics and environmental media [17,18], motivating extensive research efforts aimed at uncovering substantial principles and deriving unified frameworks for understanding animal movements and informing robotic developments [8,15,17,19–21].

Recent studies focusing on highly damped environments (e.g., viscous fluids [22], granular media [8,23], and frictional substrates [24]), where inertial effects can be ignored, have shown that undulatory locomotion can be effectively modeled within a general geometric framework known as geometric mechanics (also referred to as the "geometric phase approach") [19,20]. The concept of geometric phase was originally developed in quantum mechanics [25] and later applied to classical mechanics [26]. Specifically, Shapere and Wilczek [27] demonstrated that the geometric phase approach could provide important insights into the locomotion of microorganisms. Further, beginning in the 1980s, physicists and control theorists extended the geometric phase framework to a variety of systems moving through different environments. For example, beginning with Purcell's three-link swimmer [28], a simple model used to study locomotion in low-Reynolds-number fluids [29,30], geometric mechanics has been extended to viscous fluids [31,32] and dry granular media [19], where the dynamics can be determined analytically and empirically. More broadly, with appropriate dimension-reduction techniques, geometric mechanics has proven effective in modeling animal locomotion across diverse environments [20] and in guiding the control of limbless robots [15,32,33].

*These authors contributed equally to this work.
†Contact author: daniel.goldman@physics.gatech.edu

Although effective in modeling undulatory locomotion in highly damped environments, geometric mechanics tools are limited to linking *determined* self-deformation patterns (gaits) with their resulting locomotor performance [27]. However, in the practical control of limbless robots or the neuromechanics of elongate organisms, shape-change patterns are not directly prescribed but instead emerge from interactions between body viscoelasticity and the surrounding homogeneous or heterogeneous environment. This interaction-involved "loop" plays a central role in the gait adaptation of *Caenorhabditis elegans* [34,35] [Fig. 1(c)] and has been shown to simplify robot control in rheologically complex media [36]. To address this, Ramasamy and Hatton [37] extended the geometric framework to identify optimal gaits for compliant swimmers. The framework successfully modeled and optimized performance under system constraints for two types of proposed Purcell's three-link swimmers, each with one actuated joint and one purely elastic joint, in a viscous fluid (similar to the systems described in Ref. [38]). However, its broader applicability to physical robotic platforms remains to be demonstrated.

Similar attention has been devoted in robotics to the optimal control of systems with elastic actuation [39–43]. Inspired by the compliance observed in biological organisms, elastic actuation—achieved through actuators incorporating elastic components or soft materials—has been widely implemented in manipulators [44–46], legged robots [47–50], and exoskeletons [51–53] to mitigate external perturbations, for safer physical interactions and/or improved adaptability to complex environments. However, the added compliance complicates control by introducing nonlinear dynamics and frequency-dependent behavior, particularly in contact-rich tasks. As a result, controlling such systems often requires computationally intensive methods, which can limit their practical deployment in real-world applications [54–56].

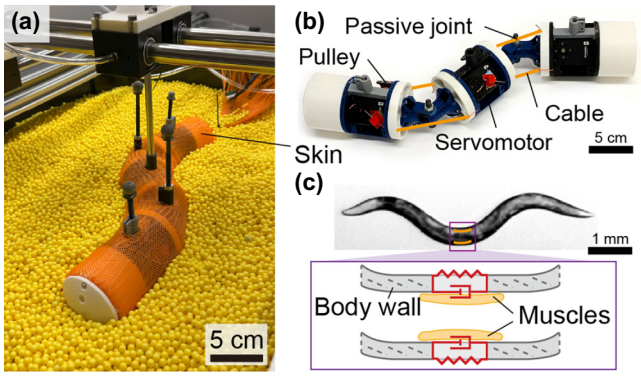

FIG. 1. Concept of body compliance in a cable-driven, three-link robophysical model and *C. elegans* nematodes. (a) The cable-driven, three-link swimmer, mounted on a gantry, was immersed in a granular medium. (b) Cable-driven, three-link swimmer robophysical model (skin off), with bilateral cables routed through pulleys and actuated by servomotors to produce in-plane bending and body compliance. (c) The nematode *C. elegans* has compliant body walls and bilateral muscles along its body.

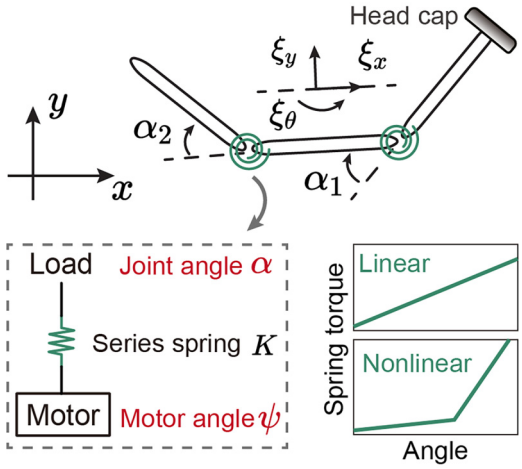

FIG. 2. Analytical three-link model with a body frame corresponding to a weighted average of the link positions and orientations. Each joint includes a motor connected in series with a spring. Insets illustrate linear and nonlinear springs, which can be captured by the model.

In this work, we develop a framework based on geometric mechanics to model and optimize the performance of compliant swimmers in overdamped environments. To achieve this, we introduce a compliant extension of Purcell's three-link swimmer by incorporating series-connected springs at both joints (as shown in Fig. 2), in which the realized gait emerges from interactions between actuation patterns, body compliance, and the environment. We first model the system dynamics using resistive force theory (RFT) and use geometric mechanics tools to predict locomotor performance. We then propose a gait optimization framework that identifies gaits that yield maximal displacement from geometric mechanics and generates their corresponding control commands through inverse body dynamics. We validate the framework by applying it to a physical cable-driven limbless robot capable of exhibiting tunable, state-dependent compliance [Figs. 1(a) and 1(b)] and demonstrate that it can accurately predict and optimize its locomotion under varied body compliance in a granular medium.

II. METHOD

A. System dynamics

The model is based on Purcell's classic three-link swimmer model, comprising three rigid segments connected in series. Body compliance is incorporated by our introducing a spring in series with each motor, as illustrated in

Fig. 2. For locomotion in highly damped environments (also referred to as "low-coasting environments" [20]), where inertial effects are typically negligible, environmental forces are assumed to be balanced by internal body compliance (spring forces). Under these assumptions, the governing equation describing system dynamics is

$$\underbrace{\mathbf{K}(\boldsymbol{\alpha})(\boldsymbol{\psi}-\boldsymbol{\alpha})}_{\text{body torque}} = \boldsymbol{\tau}_{\text{env}}(\boldsymbol{\alpha},\dot{\boldsymbol{\alpha}}), \tag{1}$$

where $\boldsymbol{\alpha} = [\alpha_1, \alpha_2]^{\mathrm{T}}$ represents the emergent shape of the swimmer (joint angles that the swimmer realize, hereafter denoted α as "emergent" joint angles), $\boldsymbol{\psi}$ denotes the shape we command the swimmer to form by actuating the cables (hereafter we call ψ the "suggested" joint angles), $\mathbf{K}(\boldsymbol{\alpha})$ is the 2×2 joint stiffness matrix, and $\boldsymbol{\tau}_{\text{env}}(\boldsymbol{\alpha},\dot{\boldsymbol{\alpha}})$ represents environmental torques acting on each joint. In this study, we present a general formulation in which the joint stiffness matrix can be either constant or explicitly state-dependent on the joint angles (Fig. 2). While both cases are considered theoretically, the robophysical realization examined in the following section uses a state-dependent stiffness.

The environmental forces acting on each link are modeled with the use of RFT, which decomposes forces into local normal and tangential components relative to the link surface. In this study, we consider locomotion in a 6 mm granular medium, which is shown to be a highly damped environment [19]. Locomotion within granular media is captured with the use of granular RFT, an effective rate-independent force model that accounts for the dependence of resistive forces on velocity direction and has successfully described undulatory locomotion in granular media [18]. To more accurately represent the real-world robophysical system, introduced in the following section, we model the body as a series of connected links without accounting for body width, while incorporating a T-shaped element at the first link to represent the head, as shown in Fig. 2.

B. Geometric mechanics

The system dynamics for a given motor command are solved on the basis of Eq. (1). In highly damped environments, where the locomotion is approximated as quasistatic, the kinematics can be estimated as

$$\boldsymbol{\xi} = \mathbf{A}(\boldsymbol{\alpha})\dot{\boldsymbol{\alpha}} = \begin{bmatrix} A_x(\boldsymbol{\alpha}) \\ A_y(\boldsymbol{\alpha}) \\ A_\theta(\boldsymbol{\alpha}) \end{bmatrix} \dot{\boldsymbol{\alpha}}, \tag{2}$$

where $\boldsymbol{\xi} = [\xi_x, \xi_y, \xi_\theta]^{\mathrm{T}}$ refers to the body velocity in forward, lateral, and rotational directions, as shown in Fig. 3(a), $\boldsymbol{\alpha}$ represents the actual joint angles as mentioned before, and $\mathbf{A}(\boldsymbol{\alpha})$ is the 3×2 local connection matrix that

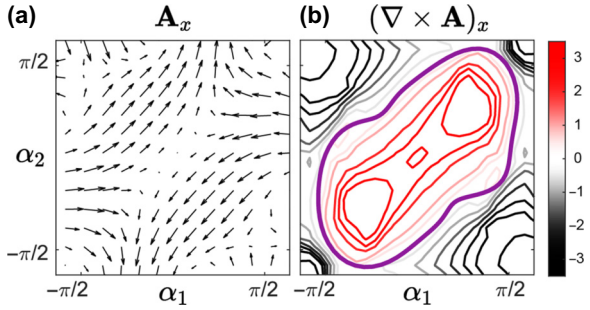

FIG. 3. Tools from geometric mechanics for modeling and optimization. (a) Local connection vector field from geometric mechanics, which maps joint velocities to body velocities and provides the foundation for displacement prediction. (b) Height function, the curl of the local connection vector field. The net displacement from a gait (purple) corresponds to the areas it encloses on the height function. The unit of the height function is body length per radian squared, and its values are scaled by a factor of 100.

maps the joint angular velocity with the body velocity linearly. Each row of the matrix represents the direction of the body velocity and can be visualized as a connection vector field in shape space as shown in Fig. 3. For viscous fluid or granular media, the local connection matrix can be analytically or numerically solved by the following force $F_{x,y}$ and torque M balance:

$$\sum_i \mathbf{F}_i(\boldsymbol{\xi},\boldsymbol{\alpha},\dot{\boldsymbol{\alpha}}) = \sum_i [F_x^i, F_y^i, M_i]^{\mathrm{T}} = 0, \tag{3}$$

where $\mathbf{F}_i$ denotes the environmental force applied on each link. With the local connection matrix, the body velocity can be calculated as the product of the connection matrix and the joint angular velocity.

For a periodic gait $\{\partial\phi : [\alpha_1(t), \alpha_2(t)], t \in (0, T]\}$, where T is the temporal period, the displacement in x, y, and rotational directions $(\Delta x, \Delta y, \Delta\theta)$ can be approximated to the first order as

$$\begin{pmatrix} \Delta x \\ \Delta y \\ \Delta\theta \end{pmatrix} \approx \int_{\partial\phi} \mathbf{A}(\boldsymbol{\alpha})\dot{\boldsymbol{\alpha}}. \tag{4}$$

Further, according to Stokes's theorem, the line integral along a closed curve $\partial\phi$ is equal to the surface integral of the curl of $\mathbf{A}(\boldsymbol{\alpha})$ over the surface enclosed by the path. Equation (4) can be derived as

$$\begin{pmatrix} \Delta x \\ \Delta y \\ \Delta\theta \end{pmatrix} \approx \iint_{\phi} \nabla \times \mathbf{A}(\boldsymbol{\alpha}) \mathrm{d}\alpha_1 \mathrm{d}\alpha_2, \tag{5}$$

where ϕ is the surface enclosed by path $\partial\psi$. $\nabla \times \mathbf{A}(\boldsymbol{\alpha})$ refers to the height function. Specifically, $(\nabla \times \mathbf{A})_x$ illustrated in Fig. 3(b) presents the forward height function,

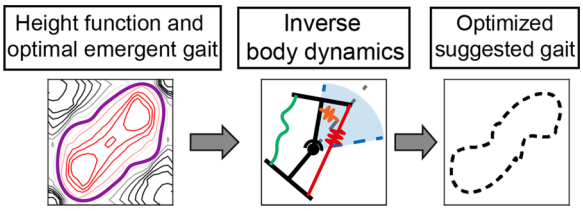

FIG. 4. Optimization flow for identifying optimal gaits with body compliance. First, the optimal emergent gait is identified by deriving the height function. Then, by incorporating the inverse body dynamics, the corresponding optimized gait is obtained.

which quantifies the net forward placement for one completed gait cycle.

Using the height function, the gait search problem becomes one of identifying a closed path in shape space that maximizes the enclosed height-function integral. Optimal displacement gait can be visually identified in the height function where the closed path maximizes the surface integral. For example, the optimal forward displacement gait in a granular medium of 6-mm-diameter plastic spheres is shown as the purple path in Fig. 3(b). Practically, gait execution is constrained by the geometric limits of the physical robot. In our experiments, each joint is limited to a range of 75°. When the calculated optimal gait exceeds this range, the values are truncated to the joint limit.

C. Gait optimization flow

The goal of this section is to identify the optimal commanded motor-angle sequence in motor space, $\boldsymbol{\psi}$, that drives the swimmer to realize an emergent joint-angle trajectory in shape space, $\boldsymbol{\alpha}$, maximizing forward displacement under body-environment interactions. We prescribed the commanded motor angles ψ_i for two-joint ($i = 1, 2$) motor space as a tenth-order Fourier series:

$$\psi_i = \sum_{p=1}^{10} a_p^i \cos\left(\frac{2\pi pt}{T}\right) + b_p^i \sin\left(\frac{2\pi pt}{T}\right), \qquad (6)$$

where T is the temporal period of the gait. The optimization flow is described in Fig. 4. To simplify the calculation we incorporate the height function from geometric mechanics. After the height function has been derived from the certain medium (viscous fluid or granular media), the optimal gait can be identified from the height function. With the optimal gait in shape space, we can directly solve the motor space parameters $\{a_1^i, \ldots, a_{10}^i, b_1^i, \ldots, b_{10}^i\}$ from Eq. (1).

III. ROBOPHYSICAL IMPLEMENTATION

A. Robophysical model development

The robophysical model used in this study is a cable-driven, three-link (two-joint) limbless swimmer. Both joints allow in-plane rotational bending, enabling the swimmer to execute planar undulatory motions. All three modules are mechanically identical, each with a length of 10 cm and a diameter of 7.5 cm. Each module consists of a three-dimensionally-printed polylactic acid outer shell that houses one DYNAMIXEL 2XL430-W250-T (ROBOTIS) actuator. This actuator contains two independently controlled servomotors, each driving a pulley with a 9.5 mm inner diameter. Nonelastic cables (Rikimura) are spooled around the pulleys to form antagonistic pairs on two sides of the joint. These cables exhibit negligible shape memory and minimal elongation under load, ensuring accurate and consistent transmission of actuation. The distal ends of the cables are anchored to the adjacent module, enabling joint motion via differential cable retraction. The swimmer is wrapped in a mesh skin made of 4-cm-inner-diameter expandable sleeving (McMaster-Carr). This outer layer smooths the body profile and prevents granular particles from entering the joint gaps, which could otherwise cause jamming or hindered motion.

B. Cable-driven scheme

To verify the modeling and optimization scheme, we introduce body compliance in the swimmer through a bilateral cable–driven scheme, which has been shown to facilitate body compliance in undulatory locomotion and thereby simplify locomotion control [36]. Specifically, each joint is actuated by two cables, whose lengths can be independently controlled as L_i^r and L_i^l for the right and left cables, respectively, with the geometric relationship illustrated in Fig. 5(a). We define a generalized compliance parameter G to control the simultaneous contraction of cables at each joint, governed by the following equations:

$$L_i^l(\psi_i) = \begin{cases} \mathcal{L}_i^l(\psi_i) & \text{if } \psi_i \le -\gamma, \\ \mathcal{L}_i^l[-\min(A_\psi, \gamma)] + l_0[\gamma + \psi_i] & \text{if } \psi_i > -\gamma, \end{cases}$$
$$L_i^r(\psi_i) = \begin{cases} \mathcal{L}_i^r(\psi_i) & \text{if } \psi_i \ge \gamma, \\ \mathcal{L}_i^r[\min(A_\psi, \gamma)] + l_0[\gamma - \psi_i] & \text{if } \psi_i < \gamma, \end{cases} \qquad (7)$$

where $\mathcal{L}_i^l$ and $\mathcal{L}_i^r$ denote the exact lengths of the left and right cables corresponding to the suggested motor angles, based on the geometry shown in Fig. 5(a). Here A_ψ is the commanded gait amplitude, l_0 is a fixed design parameter related to cable tightness, and $\gamma = (2G - 1)A_\psi$.

Within this scheme, by variation of the generalized compliance G, one cable becomes loose, while the other is tightened, as illustrated in Fig. 6(a). The loose cable defines a compliant region of the joint that can rotate freely. Depending on G, the joint exhibits different behaviors: (1) a rigid joint when $G = 0$; (2) a directionally compliant joint (e.g., $G = 0.5$), where the joint can bend in one direction but not the other; (3) a bidirectionally compliant joint (e.g., $G = 1$), where the joint can bend in both directions.

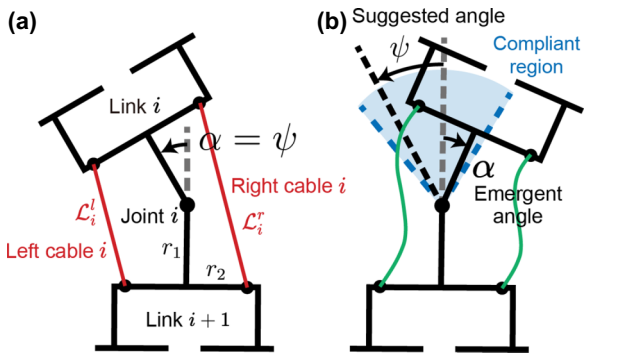

FIG. 5. Cable-driven robophysical model design and joint compliance mechanism. Bilateral cable actuation at a single joint, where (a) the left and right cables are tensioned to form the exact suggested joint angle and (b) the left and right cable are slackened to form a compliant region, so that the emergent joint angle can deviate from the suggested angle.

With the generalized compliance G, the equivalent joint stiffness becomes state dependent, as G sets the extent of the compliant angular range before cable engagement. When the actual joint angle remains within the compliant region, the swimmer's skin acts as a weak spring, restoring the joint toward the zero position [Fig. 6(b)]. When the joint angle reaches the rigid boundary (be about to move out of the compliant region), the cable tightens and introduces an additional spring in series [Fig. 6(c)]. The resulting state-dependent body compliance can therefore be expressed as

$$K(\alpha; G) = \begin{cases} k_{\text{skin}} & \text{if } \alpha \in \text{compliant region}, \\ k_{\text{skin}} + k_{\text{cable}} & \text{if } \alpha \notin \text{compliant region}, \end{cases} \quad (8)$$

where k_{skin} and k_{cable} are the stiffness values of the skin and the cable, respectively, as measured in previous work [36]. Note that the compliant region (the blue region in Fig. 6) depends on the prescribed G and the commanded joint angle ψ. Equation (8) therefore provides the constitutive link between the control parameter G and the effective joint stiffness K, which is then incorporated into the system dynamics in Eq. (1) to determine emergent joint motion and locomotor performance.

In summary, we model the cable-driven actuation of our robophysical system as a state-dependent joint stiffness $K(\alpha; G)$ governed by the programmed generalized compliance G. The generalized body compliance controls the relative extent of the low-stiffness regime (skin only) and the stiffened regime in which the cable is engaged. With this effective state-dependent joint stiffness, we can incorporate it into the framework of Eq. (1) to model and optimize our robophysical system.

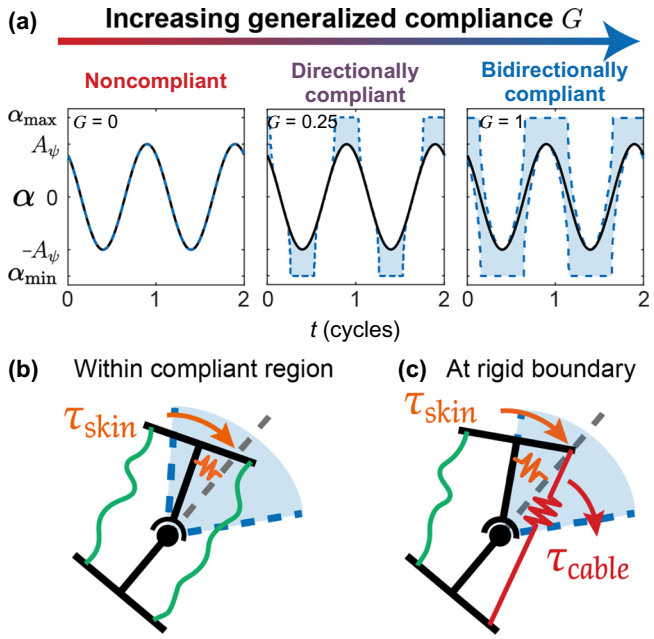

FIG. 6. Effect of generalized compliance G on joint behavior. (a) Emergent joint angle trajectories α across different compliance regimes: rigid (noncompliant, $G = 0$), directionally compliant ($G = 0.25$), and bidirectionally compliant ($G = 1$). Compliance increases the range of joint motion within which the suggested angle ψ can deviate, illustrated by shaded blue regions. (b) Within the compliant region, the joint is governed primarily by the skin's restoring torque τ_{skin}. (c) At the rigid boundary, cable tension engages, introducing an additional restoring torque τ_{cable} that stiffens the joint response.

IV. EXPERIMENTS

Experiments were conducted in a test bed filled with plastic spheres (6 mm diameter), which served as the granular environment. To constrain the swimmer's motion to a horizontal plane and maintain a consistent depth, we designed a custom gantry system incorporating air bearings. The system includes two orthogonal linear air bearings (New Way Air Bearings) that provide nearly frictionless translation along the x- and y-axes, and a rotational ball bearing enabling smooth in-plane rotation as shown in Fig. 7. The swimmer is attached to the gantry via a vertical shaft whose lower end is fixed to a rigid connector mounted at the center of the middle link. This mechanical coupling ensures that the swimmer remains suspended at a constant height, while allowing free planar motion. The overall setup minimizes mechanical resistance, eliminates vertical drag or sinkage, and enables repeatable locomotion trials within the granular bed.

To track the motion of the swimmer during experiments, we uniformly attached four infrared reflective markers along its body: one at the head, two at joints, and one at the tail. An OptiTrack motion capture system with six OptiTrack Flex 13 cameras was used to track

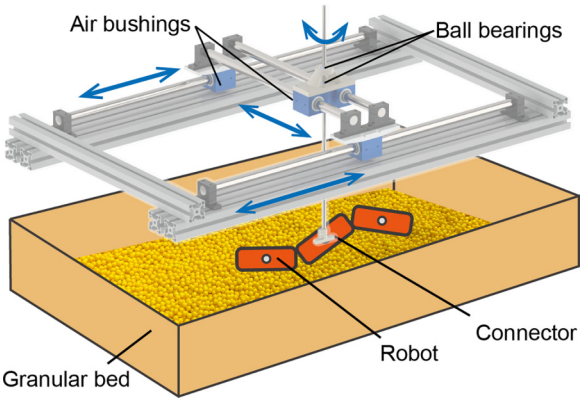

FIG. 7. Experimental setup for robophysical experiments in granular media. The robophysical model is immersed in a granular medium and mounted on a gantry, which constrains its motion to the horizontal plane, while allowing both translation and rotation.

the three-dimensional positions of the markers at a frame rate of 120 s^{-1}. We recorded trajectories of swimmer movement and calculated displacements and body shape patterns to evaluate locomotor performance.

In each experiment, the swimmer was positioned such that its entire body was fully immersed in the granular medium, with the top edge maintained at a depth of 1 cm beneath the surface. For every gait tested, the swimmer executed seven full cycles. To eliminate the effects of transient dynamics, only the final five cycles were included in the analysis. Each experiment was conducted five times, and we report averaged results with standard deviation across trials.

V. RESULTS

A. Verification of system dynamics for shape prediction with body compliance

A critical first step in validating our framework is to confirm that the system dynamics model [Eq. (1)] correctly predicts the actual body shapes that emerge when motor commands are filtered through compliance and environmental interactions. To test this, we prescribed a nominal circular gait in motor space, following the gait equations

$$\psi_1(t) = A_\psi \cos(2\pi\omega t),$$
$$\psi_2(t) = A_\psi \sin(2\pi\omega t). \tag{9}$$

Specifically, we selected $A_\psi = \pi/3$ and $\omega = 0.1$ Hz (one gait cycle takes 10 s).

Before summarizing compliance-induced deformations of emergent gaits in shape space, we first illustrate how these emergent shape trajectories translate into physical locomotor motion. Figure 8 presents a representative example for a circular-input gait at moderate compliance ($G = 0.75$). The top row shows time-ordered snapshots

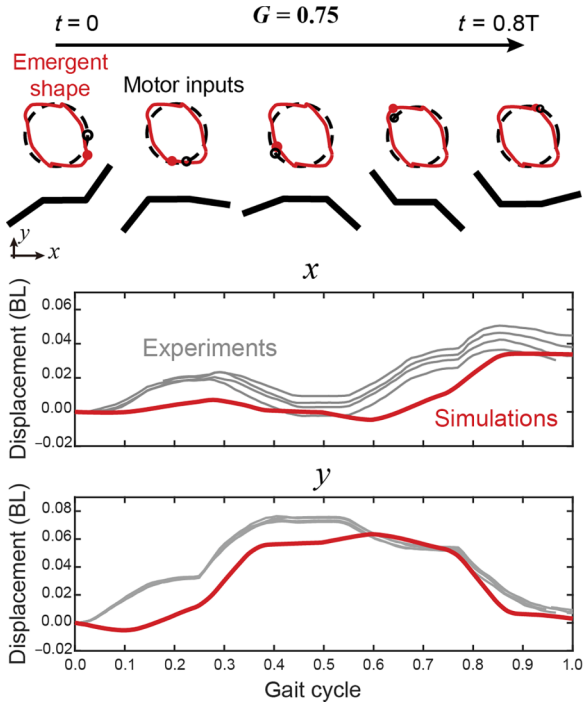

FIG. 8. Emergent shape-space dynamics and resulting locomotor performance for circular-input gaits. Top: Time-ordered snapshots of motor inputs and resulting body shapes over one gait cycle for a circular-input gait at $G = 0.75$, shown from $t = 0$ to $t = 0.8T$. Dashed black outlines show the suggested joint angles from motors, and the red curves indicate the emergent joint angles from simulation. Middle and bottom: Corresponding cumulative displacements in the laboratory x and y directions [in body lengths (BL)] over the gait cycle, comparing experiments (gray) and simulations (red). The close agreement between simulated and experimental shape evolution leads to similar displacement histories, illustrating how emergent shape-space trajectories govern physical locomotor performance.

of the swimmer over a gait cycle, comparing the suggested motor-space joint angles with the emergent joint angles predicted by the system dynamics model. Because of body compliance and environmental interactions, the realized joint motion deviates from the nominal circular command, producing a distorted but repeatable trajectory in shape space. The resulting shape evolution generates net displacement, as reflected in the cumulative body motion in the laboratory x and y directions shown below in Fig. 8. Simulated displacement histories closely match experimental measurements, demonstrating that the predicted emergent shape dynamics not only capture joint-level deformation but also directly account for the resulting locomotor motion.

We then examined the resulting trajectories in shape space under different levels of generalized compliance G. Representative cases are shown in Fig. 9. With no compliance ($G = 0$), the swimmer can accurately execute the prescribed gait commands where its trajectory in the shape

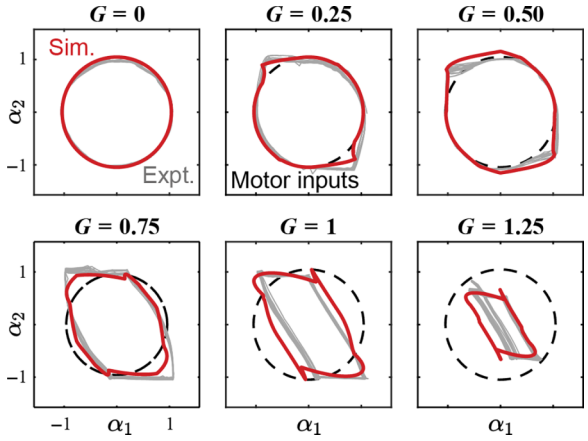

FIG. 9. Validation of system dynamics for predicting emergent shapes under compliance. Emergent gait trajectories in shape space (α_1-α_2) for increasing generalized compliance G. Dashed circles indicate prescribed circular motor inputs, gray lines show experimental measurements, and red lines denote simulation predictions (Sim.). With no compliance ($G = 0$), emergent gaits closely follow the commanded circular inputs, while body compliance causes distorted and collapsed trajectories. Simulation results capture the deformation trends observed in experiments across all compliance regimes.

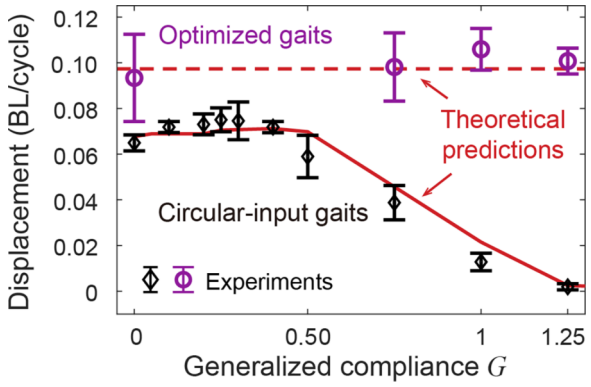

FIG. 10. Verification of locomotor performance predictions under gait optimization and varied body compliance. Quantitative comparison of displacement per cycle [in body lengths (BL)] as a function of generalized compliance G for circular-input and optimized gaits. Predictions from the geometric mechanics height-function integral (red) closely match experimental measurements (black points; error bars denote standard deviation).

space (α_1-α_2 space) forms a perfect circle. At low compliance ($G = 0.25$), the emergent gait closely followed the commanded circle, indicating that the motor commands were faithfully transmitted to the joints with little deformation. At moderate compliance ($G = 0.75$), the emergent gait deviated substantially from the nominal circular path, reflecting the growing influence of environmental torques relative to joint stiffness. At high compliance ($G = 1.25$), the emergent gait collapsed into a much smaller, distorted loop, demonstrating that environmental forces dominate the effective shape dynamics when the joints are highly compliant. The experimental videos can be found in Supplemental Material [57].

Across all conditions, the predicted shape trajectories generated by our dynamics model (red) showed excellent agreement with experimentally observed trajectories (gray), capturing both the degree and the direction of gait deformation as compliance increased. This agreement demonstrates that the system dynamics model accurately encodes the interaction between motor commands, joint compliance, and environmental resistance. In effect, the model provides a quantitative description of how compliance reshapes commanded motor gaits into realized body motions in shape space.

B. Verification of the full geometric mechanics model for locomotor performance prediction

While the dynamics model captures how commanded gaits are transformed into emergent trajectories, locomotor performance depends on how these trajectories interact with environmental forces to generate net displacement. To assess whether our framework can also predict performance outcomes, we quantified the displacement per cycle as a function of generalized compliance G (Fig. 10).

Geometric mechanics was used to derive the height function (red), which encodes the geometric phase associated with a closed trajectory in shape space and predicts the net displacement resulting from each gait cycle. The relationship between compliance and performance was not strictly monotonic. In the low-compliance regime ($G \approx 0.25$), performance was nearly unchanged compared with performance in the noncompliant case and in some conditions was even slightly higher. This occurred because environmental perturbations naturally distorted the commanded circular gait in a way that favored forward locomotion; in terms of the height function, the deformed trajectory enclosed more positive area, which increased net displacement. At higher compliance levels, however, performance declined sharply. As gait amplitude collapsed, the enclosed area in the height function shrank, leading to reduced displacement per cycle.

Experimental measurements (black) closely matched the height-function predictions, reproducing the initial plateau or slight improvement at low compliance and the drop-off at higher compliance. These results confirm that our framework predicts not only the deformation of gait trajectories but also their performance consequences. They also show that an excessive compliance ultimately reduces effectiveness in viscous fluid and granular media. In particular, Fig. 9 demonstrates that the system dynamics model captures the detailed deformation of gait trajectories across compliance regimes, while Fig. 10 summarizes the resulting performance trends. This agreement underscores the ability

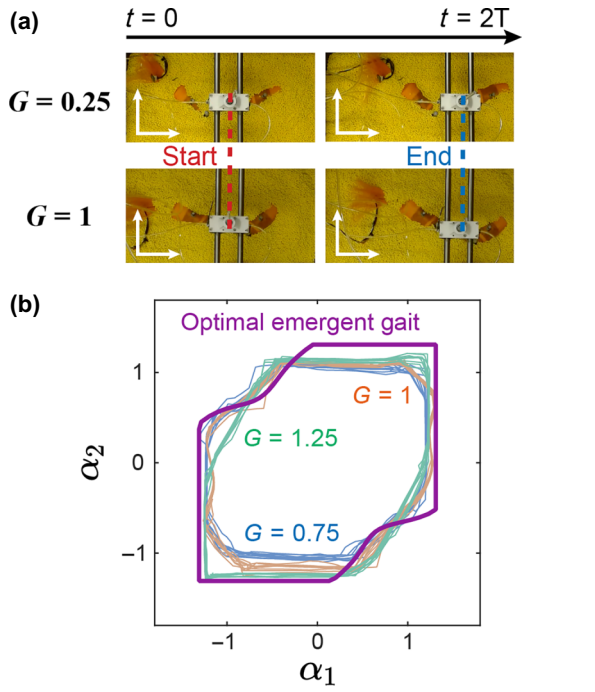

FIG. 11. Gait optimization yields robust emergent locomotion across body compliance. (a) Representative experimental snapshots of the swimmer at the start ($t = 0$) and end ($t = 2T$) of two gait cycles for low ($G = 0.25$) and high ($G = 1$) generalized compliance. Dashed lines indicate initial (red) and final (blue) body positions, illustrating comparable net displacement despite large differences in body compliance. (b) Emergent gait trajectories in shape space (α_1, α_2) for optimized motor inputs at different compliance values ($G = 0.75$, 1, and 1.25). Although body compliance varies, the resulting emergent gaits collapse onto a common trajectory that closely follows the theoretically optimal gait (purple), demonstrating compliance-invariant gait emergence under optimization.

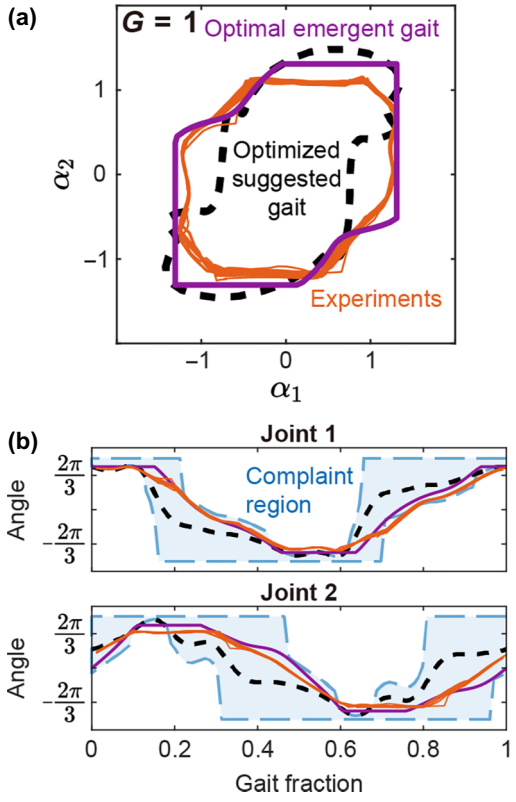

FIG. 12. Execution of optimized gaits in compliant swimmers. (a) Shape-space trajectories $G = 1$. The optimized suggested gait (dashed black line) differs substantially from the theoretical optimal emergent gait (purple line), and by executing the optimized suggested gait, the swimmer can successfully realize the optimal emergent gait (orange line). (b) Joint angle traces over one gait cycle. The emergent joint angles (orange lines) follow the optimal trajectories (purple lines), demonstrating that environmental perturbations and compliance are harnessed to reinforce performance.

of our framework to predict how motor commands generate emergent body shapes under compliance in granular media.

C. Gait optimization with the proposed framework

While circular-input gaits provided a convenient baseline to test our model, they did not achieve optimal locomotor performance across different compliance levels. In particular, performance declined sharply as compliance increased, even though the underlying system dynamics were accurately predicted. To address this limitation, we used our proposed optimization framework, which combines system dynamics, resistive force theory, and geometric mechanics to search for the input (commanding) gaits that maximize displacement given the swimmer's compliance.

Overall, Fig. 10 compares the displacement of circular suggested gaits (black points, red curve) with that of optimized suggested gaits (purple points). Circular gaits exhibited performance that was high only in the rigid or near-rigid regime and degraded rapidly with increasing compliance. In contrast, optimized suggested gaits maintained consistently high performance, nearly doubling the displacement relative to circular gaits in the compliant regime. Theoretical predictions and experimental measurements were in close agreement, confirming that the optimization framework identifies gaits that recover performance otherwise lost to compliance.

Specifically, we first identified the theoretical optimal emergent gait using RFT and geometric mechanics models, and then applied the inverse system dynamics to determine the corresponding suggested motor commands for each compliance value G. Our deploying these optimized suggested gaits on the swimmer enabled it to realize the optimal emergent gait and maintain high performance. Figure 11(b) presents a collection of emergent gait trajectories across different G values. With $G = 1$ as an example, the optimized suggested gait [dashed black line in Fig.

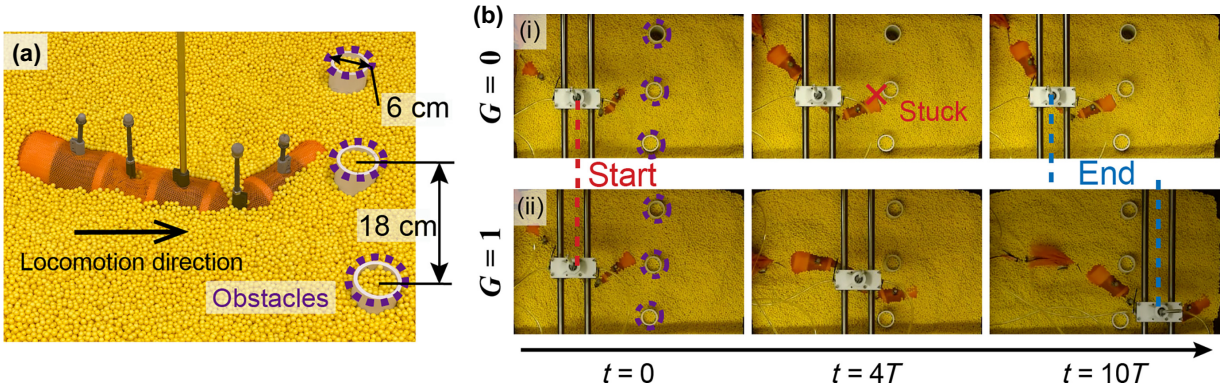

FIG. 13. An optimized gait with body compliance enables the robot to traverse obstacles. (a) Three cylindrical rigid obstacles immersed in the granular medium. (b)(i) When executing the optimized gait without body compliance ($G = 0$), the robot becomes stuck because of obstacles in the granular medium. (b)(ii) With body compliance ($G = 1$), the robot executing the optimized gait successfully passes through the obstacles while maintaining its speed.

12(a)] differs substantially from the circular input, and the swimmer reliably executed the optimal emergent gait trajectory in experiments (see also Video 2 in Supplemental Material [57]). Joint angle traces further confirm that the optimized suggested gait effectively leverages compliant regions of the dynamics [Fig. 12(b)], shaping motor inputs so that environmental perturbations naturally reinforce forward locomotion.

Together, these results demonstrate that optimization does not simply "fix" the limitations introduced by compliance but instead codesigns gaits with compliance. Without optimization, compliance might appear disadvantageous because naive circular inputs produce emergent gait loops that shrink or distort in shape space, reducing enclosed area and locomotor performance. Unlike rigid robots, which transmit environmental disturbances directly to their actuators and therefore require complex sensing and control to remain stable, compliant robots can passively absorb shocks, adapt their body shape when moving through granular media or clutter, and reduce the burden on active control. In this way, compliance provides a built-in form of mechanical intelligence that increases robustness across environments. Beyond robotics, incorporating compliance also increases the biological relevance of our robophysical models, since animals rely on body elasticity for effective locomotion. Thus, optimization enables compliant robots to achieve high performance while simultaneously establishing them as powerful physical models for studying the role of compliance in biological systems.

D. Optimized compliance for robust obstacle navigation

While the previous sections demonstrated how compliance reshapes motor commands and how optimization can recover performance in homogeneous environments, the true advantage of compliance becomes evident in cluttered settings. To test this, we introduced a row of rigid pillars embedded in a granular medium [Fig. 13(a) and Video 3 in Supplemental Material [57]], where the swimmer was required to pass through the openings between pillars.

When operated with no compliance ($G = 0$), the swimmer jammed upon its contacts with the obstacles as shown in Fig. 13(b)(i). With a rigid-body configuration, the swimmer was unable to reconfigure its shape to exploit the available openings. In some cases, external contact forces were transmitted directly to the actuators, potentially driving them toward torque limits and further preventing forward progression. By contrast, with high compliance ($G = 1$), the swimmer was able to negotiate the obstacles smoothly, as illustrated in Fig. 13(b)(ii). Passive joint flexibility allowed the body to bend around the pillars and "flow" through the available gaps without requiring explicit sensing or contact modeling. To further explain the role of body compliance in facilitating obstacle traversal, we examined the joint-level responses of the robot executing the optimized gait. Figure 14(a) shows at the head that compliance allows the joint to adapt passively upon contact with an obstacle, producing a hooking response that effectively leverages the obstacle to aid forward motion. This behavior is reflected in the joint angle trajectory, which deviates from the prescribed optimal gait during contact. At the tail [Fig. 14(b)], compliance enables passive deflection as the segment encounters an obstacle, thereby reducing resistive forces that would otherwise impede motion.

It is worth noting that compliance alone is not sufficient for obstacle navigation. Without gait optimization, the compliant swimmer could not achieve effective forward speed in homogeneous media, and thus would also fail to make useful progress in cluttered environments. Our optimization framework resolves this limitation by identifying motor commands that maximize displacement with

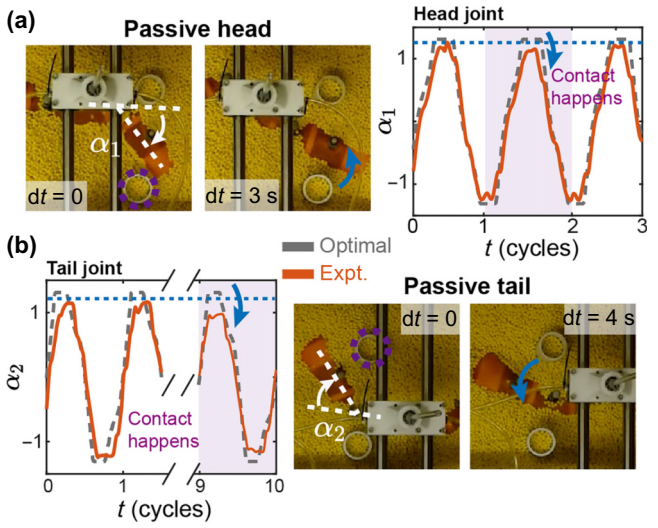

FIG. 14. Passive responses from compliance augment locomotion capabilities. (a) Compliance in the head joint enables a passive hooking response that aids locomotion upon contact with obstacles. (b) Compliance in the tail joint allows passive deflection, reducing resistance from obstacles.

varied G. With optimized gaits, the swimmer maintains high speed, and compliance then naturally takes over the task of negotiating unpredictable obstacle contacts.

This result illustrates a practical control principle: in real-world environments, it is impossible to explicitly model every unknown contact. Instead, robots should be optimized for performance with compliance in homogeneous media, and then rely on compliance to handle unmodeled obstacle interactions. This approach exemplifies the philosophy of mechanical intelligence in robotics, in which passive body mechanics are deliberately leveraged to offload control and increase robustness. In this way, compliance transforms from a performance liability into a robust locomotor strategy, allowing swimmers to move effectively through clutter, where purely rigid robots fail.

VI. CONCLUSION

In this work, we developed and experimentally validated a unified framework for modeling, analyzing, and optimizing the locomotion of compliant cable-driven limbless swimmers in highly damped environments. Starting from Purcell's three-link swimmer, we introduced body compliance by incorporating series elastic elements into the system dynamics, which allowed the model to map commanded motor-angle sequences, $\psi(t)$, to emergent joint-angle sequences, $\alpha(t)$. Coupled with resistive force theory and geometric mechanics, this framework enabled us to predict how compliance reshapes commanded gaits and how these emergent trajectories interact with the environment to generate locomotion. Through robophysical experiments with a three-link swimmer in a granular medium, we verified that the framework accurately predicts both gait deformation and locomotor performance. Finally, we applied the optimization pipeline to identify gaits that maximize displacement under different levels of compliance and showed that swimmers executing these optimized gaits achieve consistently high performance across compliance regimes. Our results extend the gait design framework of geometric mechanics from systems with prescribed shape control to those in which shape emerges from interactions between the environment and body elasticity. Furthermore, geometric mechanics plays a vital role in simplifying the search for optimal control strategies.

Beyond these, this study provides deeper insight into the role of compliance in limbless locomotion. Our findings reveal that, beyond its well-recognized benefits for interacting with environmental heterogeneity, compliance should not be viewed solely as a constraint or deficiency even in homogeneous environments. While naive circular gaits degrade with increasing compliance, optimized gaits exploit compliance to increase robustness and adaptability. Unlike rigid robots, which transmit external disturbances directly to actuators and therefore require sophisticated sensing and control to maintain stability, compliant robots can passively absorb contacts, adapt their body shape to cluttered or granular terrain, and reduce control complexity. This passive adaptability represents a form of mechanical intelligence that allows robots to offload part of the locomotor "control problem" to their body mechanics. This work further shows how compliance can be implemented while still achieving optimal performance, allowing compliance to act as an additional design benefit rather than a drawback in homogeneous environments. Moreover, embedding compliance into robotic platforms strengthens their connection to biological systems, where body elasticity plays an important role in effective movement.

This work opens up several new directions for advancing the study of compliant undulatory locomotion. First, the framework can be extended to more diverse robot morphologies, such as swimmers with longer bodies or additional joints, and to more complex three-dimensional gaits that better capture the richness of animal locomotion. Second, while this study focused on displacement performance, future efforts should investigate the energetic consequences of compliance, examining whether compliant bodies enable more-energy-efficient locomotion by reducing actuation effort or exploiting passive body dynamics. Third, by application of this framework in conjunction with comparative biological studies, compliant robophysical models could serve as experimental platforms for testing biomechanical hypotheses and exploring how animals leverage compliance for robustness and efficiency. Together, these directions highlight the potential of compliance-aware geometric mechanics not only to advance the design of resilient robots but also to deepen

our understanding of limbless locomotion in the natural world.

ACKNOWLEDGMENTS

The authors thank Ross L. Hatton for helpful discussion. The authors are grateful for funding from Army Research Office Grants No. W911NF-11-1-0514 and No. W911NF-20-1-0129. The authors acknowledge the use of ChatGPT (OpenAI) for language editing.

DATA AVAILABILITY

The data that support the findings of this article are not publicly available. The data are available from the authors upon reasonable request.

[1] J. Gray, The mechanism of locomotion in snakes, J. Exp. Biol. **23**, 101 (1946).
[2] D. L. Hu, J. Nirody, T. Scott, and M. J. Shelley, The mechanics of slithering locomotion, Proc. Natl. Acad. Sci. **106**, 10081 (2009).
[3] B. C. Jayne, Kinematics of terrestrial snake locomotion, Copeia **1986**, 915 (1986).
[4] H. C. Astley, C. Gong, J. Dai, M. Travers, M. M. Serrano, P. A. Vela, H. Choset, J. R. Mendelson III, D. L. Hu, and D. I. Goldman, Modulation of orthogonal body waves enables high maneuverability in sidewinding locomotion, Proc. Natl. Acad. Sci. **112**, 6200 (2015).
[5] J. L. Tingle, K. L. Garner, and H. C. Astley, Functional diversity of snake locomotor behaviors: A review of the biological literature for bioinspiration, Ann. N. Y. Acad. Sci. **1533**, 16 (2024).
[6] G. B. Gillis, Environmental effects on undulatorylLocomotion in the American eel *Anguilla rostrata*: Kinematics in water and on land, J. Exp. Biol. **201**, 949 (1998).
[7] E. D. Tytell and G. V. Lauder, The hydrodynamics of eel swimming: I. Wake structure, J. Exp. Biol. **207**, 1825 (2004).
[8] R. D. Maladen, Y. Ding, C. Li, and D. I. Goldman, Undulatory swimming in sand: subsurface locomotion of the sandfish lizard, Science **325**, 314 (2009).
[9] B. Chong, T. Wang, E. Erickson, P. J. Bergmann, and D. I. Goldman, Coordinating tiny limbs and long bodies: Geometric mechanics of lizard terrestrial swimming, Proc. Natl. Acad. Sci. **119**, e2118456119 (2022).
[10] S. Hirose and M. Mori, in *2004 IEEE International Conference on Robotics and Biomimetics* (IEEE, 2004), pp. 1–7.
[11] A. A. Transeth, R. I. Leine, C. Glocker, K. Y. Pettersen, and P. Liljebäck, Snake robot obstacle-aided locomotion: Modeling, simulations, and experiments, IEEE Trans. Robot. **24**, 88 (2008).
[12] A. Crespi and A. J. Ijspeert, Online optimization of swimming and crawling in an amphibious snake robot, IEEE Trans. Robot. **24**, 75 (2008).
[13] C. Wright, A. Johnson, A. Peck, Z. McCord, A. Naaktgeboren, P. Gianfortoni, M. Gonzalez-Rivero, R. Hatton, and H. Choset, in *2007 IEEE/RSJ International Conference on Intelligent Robots and Systems* (IEEE, 2007), pp. 2609–2614.
[14] A. Crespi, K. Karakasiliotis, A. Guignard, and A. J. Ijspeert, Salamandra robotica II: An amphibious robot to study salamander-like swimming and walking gaits, IEEE Trans. Robot. **29**, 308 (2013).
[15] B. Chong, T. Wang, J. M. Rieser, B. Lin, A. Kaba, G. Blekherman, H. Choset, and D. I. Goldman, Frequency modulation of body waves to improve performance of sidewinding robots, Int. J. Rob. Res. **40**, 1547 (2021).
[16] R. D. Maladen, Y. Ding, P. B. Umbanhowar, and D. I. Goldman, Undulatory swimming in sand: experimental and simulation studies of a robotic sandfish, Int. J. Rob. Res. **30**, 793 (2011).
[17] Z. V. Guo and L. Mahadevan, Limbless undulatory propulsion on land, Proc. Natl. Acad. Sci. **105**, 3179 (2008).
[18] J. Aguilar, T. Zhang, F. Qian, M. Kingsbury, B. McInroe, N. Mazouchova, C. Li, R. Maladen, C. Gong, M. Travers, *et al*., A review on locomotion robophysics: The study of movement at the intersection of robotics, soft matter and dynamical systems, Rep. Prog. Phys. **79**, 110001 (2016).
[19] R. L. Hatton, Y. Ding, H. Choset, and D. I. Goldman, Geometric visualization of self-propulsion in a complex medium, Phys. Rev. Lett. **110**, 078101 (2013).
[20] J. M. Rieser, B. Chong, C. Gong, H. C. Astley, P. E. Schiebel, K. Diaz, C. J. Pierce, H. Lu, R. L. Hatton, H. Choset, *et al*., Geometric phase predicts locomotion performance in undulating living systems across scales, Proc. Natl. Acad. Sci. **121**, e2320517121 (2024).
[21] N. Charles, R. Chelakkot, M. Gazzola, B. Young, and L. Mahadevan, Topological dynamics of rapid non-planar gaits in slithering snakes, Nat. Phys. **21**, 856 (2025).
[22] H. C. Fu, T. R. Powers, and C. W. Wolgemuth, Theory of swimming filaments in viscoelastic media, Phys. Rev. Lett. **99**, 258101 (2007).
[23] H. Marvi, C. Gong, N. Gravish, H. Astley, M. Travers, R. L. Hatton, J. R. Mendelson III, H. Choset, D. L. Hu, and D. I. Goldman, Sidewinding with minimal slip: Snake and robot ascent of sandy slopes, Science **346**, 224 (2014).
[24] B. Chong, J. He, S. Li, E. Erickson, K. Diaz, T. Wang, D. Soto, and D. I. Goldman, Self-propulsion via slipping: Frictional swimming in multilegged locomotors, Proc. Natl. Acad. Sci. **120**, e2213698120 (2023).
[25] M. Berry, The geometric phase, Sci. Am. **259**, 46 (1988).
[26] J. E. Marsden, R. Montgomery, and T. S. Raţiu, *Reduction, Symmetry, and Phases in Mechanics* (American Mathematical Soc., Providence, RI, USA, 1990), Vol. 436.
[27] A. Shapere and F. Wilczek, Self-propulsion at low Reynolds number, Phys. Rev. Lett. **58**, 2051 (1987).
[28] E. M. Purcell, Life at low Reynolds number, Am. J. Phys. **45**, 3 (1977).
[29] L. E. Becker, S. A. Koehler, and H. A. Stone, On self-propulsion of micro-machines at low Reynolds number: Purcell's three-link swimmer, J. Fluid Mech. **490**, 15 (2003).
[30] D. Tam and A. E. Hosoi, Optimal stroke patterns for Purcell's three-link swimmer, Phys. Rev. Lett. **98**, 068105 (2007).

[31] R. L. Hatton and H. Choset, Geometric swimming at low and high Reynolds numbers, IEEE Trans. Robot. **29**, 615 (2013).
[32] S. Ramasamy and R. L. Hatton, The geometry of optimal gaits for drag-dominated kinematic systems, IEEE Trans. Robot. **35**, 1014 (2019).
[33] B. Chong, T. Wang, L. Bo, S. Li, P. C. Muthukrishnan, J. He, D. Irvine, H. Choset, G. Blekherman, and D. I. Goldman, Optimizing contact patterns for robot locomotion via geometric mechanics, Int. J. Rob. Res. **42**, 859 (2023).
[34] C. J. Pierce, D. Irvine, L. Peng, X. Lu, H. Lu, and D. I. Goldman, Dispersion relations for active undulators in overdamped environments, Phys. Rev. E (2026).
[35] C. J. Pierce, Y. Ding, L. Peng, X. Lu, B. Chong, H. Lu, and D. I. Goldman, Neuromechanical phase lags and gait adaptation in the nematode *C. elegans*, PRX Life **3**, 023001 (2025).
[36] T. Wang, C. Pierce, V. Kojouharov, B. Chong, K. Diaz, H. Lu, and D. I. Goldman, Mechanical intelligence simplifies control in terrestrial limbless locomotion, Sci. Rob. **8**, eadi2243 (2023).
[37] S. Ramasamy and R. L. Hatton, Optimal gaits for drag-dominated swimmers with passive elastic joints, Phys. Rev. E **103**, 032605 (2021).
[38] A. Zigelman, G. Ben Zvi, and Y. Or, Dynamics of Purcell-type microswimmers with active-elastic joints, Phys. Rev. E **110**, 014207 (2024).
[39] G. A. Pratt and M. M. Williamson, in *Proceedings 1995 IEEE/RSJ international conference on intelligent robots and systems. Human robot interaction and cooperative robots* (IEEE, 1995), Vol. 1, pp. 399–406.
[40] B. Vanderborght, A. Albu-Schäffer, A. Bicchi, E. Burdet, D. G. Caldwell, R. Carloni, M. Catalano, O. Eiberger, W. Friedl, G. Ganesh, *et al*., Variable impedance actuators: A review, Rob. Auton. Syst. **61**, 1601 (2013).
[41] S. P. Chhatoi, M. Pierallini, F. Angelini, C. Mastalli, and M. Garabini, Optimal control for articulated soft robots, IEEE Trans. Robot. **39**, 3671 (2023).
[42] O. Yasa, Y. Toshimitsu, M. Y. Michelis, L. S. Jones, M. Filippi, T. Buchner, and R. K. Katzschmann, An overview of soft robotics, Annu. Rev. Control Rob. Auton. Syst. **6**, 1 (2023).
[43] T. Wang, J. Whitman, M. Travers, and H. Choset, in *2020 American Control Conference (ACC)* (IEEE, 2020).
[44] J. Lin, J. Ke, R. Xiao, X. Jiang, M. Li, X. Xiao, and Z. Guo, Bioinspired bidirectional stiffening soft actuators enable versatile and robust grasping, Soft Rob. **11**, 494 (2024).
[45] T. Wang, L. Ge, and G. Gu, Programmable design of soft pneu-net actuators with oblique chambers can generate coupled bending and twisting motions, Sens. Actuat. A: Phys. **271**, 131 (2018).
[46] D. Mura, M. Barbarossa, G. Dinuzzi, G. Grioli, A. Caiti, and M. G. Catalano, A soft modular end effector for underwater manipulation: A gentle, adaptable grasp for the ocean depths, IEEE Rob. Autom. Lett. **25**, 45 (2018).
[47] M. Hutter, C. Gehring, D. Jud, A. Lauber, C. D. Bellicoso, V. Tsounis, J. Hwangbo, K. Bodie, P. Fankhauser, M. Bloesch, *et al*., in *2016 IEEE/RSJ international conference on intelligent robots and systems (IROS)* (IEEE, 2016), pp. 38–44.
[48] B. Chong, J. He, D. Soto, T. Wang, D. Irvine, G. Blekherman, and D. I. Goldman, Multilegged matter transport: A framework for locomotion on noisy landscapes, Science **380**, 509 (2023).
[49] J. Lin, Z. Guo, and A. Badri-Spröwitz, in *2025 IEEE International Conference on Robotics and Automation (ICRA)* (IEEE, 2025), pp. 15936–15942.
[50] A. Badri-Spröwitz, A. Aghamaleki Sarvestani, M. Sitti, and M. A. Daley, BirdBot achieves energy-efficient gait with minimal control using avian-inspired leg clutching, Sci. Rob. **7**, eabg4055 (2022).
[51] W. Qian, J. Liao, L. Lu, L. Ai, M. Li, X. Xiao, Z. Guo, CURER: A lightweight cable-driven compliant upper limb rehabilitation exoskeleton robot, IEEE/ASME Trans. Mechatron. **28**, 1730 (2022).
[52] M. S. Cherry, S. Kota, A. Young, and D. P. Ferris, Running with an elastic lower limb exoskeleton, J. Appl. Biomech. **32**, 269 (2016).
[53] S. H. Collins, M. B. Wiggin, and G. S. Sawicki, Reducing the energy cost of human walking using an unpowered exoskeleton, Nature **522**, 212 (2015).
[54] M. Schumacher, J. Wojtusch, P. Beckerle, and O. Von Stryk, An introductory review of active compliant control, Rob. Auton. Syst. **119**, 185 (2019).
[55] C. Alessi, C. Agabiti, D. Caradonna, C. Laschi, F. Renda, and E. Falotico, Rod models in continuum and soft robot control: A review, arXiv:2407.05886.
[56] D. A. Haggerty, M. J. Banks, E. Kamenar, A. B. Cao, P. C. Curtis, I. Mezić, and E. W. Hawkes, Control of soft robots with inertial dynamics, Sci. Rob. **8**, eadd6864 (2023).
[57] See Supplemental Material at http://link.aps.org/supplemental/10.1103/pbkh-py5h for detailed videos and additional information.